

A Dual Fabry-Perot Based Imaging Spectrometer for the National Large Solar Telescope

B. Ravindra and Ravinder Kumar Banyal
Indian Institute of Astrophysics
Koramangala, Bengaluru-560034
ravindra@iiap.res.in & banyal@iiap.res.in

1 Abstract

This report provides a detailed design of a dual Fabry-Perot based narrow band imaging system intended to make observations of solar atmosphere at visible and near infrared wavelengths. The narrow band imager will serve as one of the back end instrument planned for a proposed 2m class National Large Solar Telescope (NLST) by Indian Institute of Astrophysics. The narrow band imager comprises an air spaced, high reflectivity, large free spectral range Fabry-Perot interferometer. The instrument will have a spectral resolution of about $40 \text{ m}\text{\AA}$ to provide narrow band images of the solar atmosphere. The dopplergrams can also be made at a spatial resolution of $0.06 \text{ arc-sec/pixel}$. By combining it with the polarimeter, the narrow band imager can also provide magnetograms. Several simulations and numerical studies are carried out to arrive at the instrument design. The study of the important design parameters including optimum spacing ratio, field-of-view, optical layout, spectral and spatial resolution, signal-to-noise ratio etc is presented in detail. Finally, a comparison between the proposed instrument and similar instruments used in other solar observatories around the world is also made.

2 Introduction

National Large Solar Telescope (NLST) is being proposed, by the Indian Institute of Astrophysics (IIA), as a 2-m class next generation telescope to study the dynamics of the solar atmosphere (especially photosphere and chromosphere). The telescope will be placed in a suitable location in India where the sky and the atmospheric conditions will allow the maximum output from this instrument. More details of the NLST can be obtained from Singh (2008). The telescope will also be equipped with a high order adaptive optics system to correct the image degradation resulting from the atmospheric turbulence. The potential of this instrument can be maximized with state-of-the-art back-end instruments. NLST equipped with high class back-end instruments, that will

not only help the solar community in solving many outstanding scientific problems in solar physics, but also attract many young researchers to undertake challenging areas of research in solar physics. One such potential back-end instrument is a narrow-band imager providing high contrast images of the solar atmosphere at various wavelengths in the visible spectrum. This report is to build an imaging spectrograph using Fabry-Perot (FP) etalon in tandem. The proposed instrument will be capable of fast narrow band imaging at multiple wavelengths in the visible and near Infra-red spectrum. Addition of a polarimetric capability, which will be carried out as a separate project, would further enhance the scientific output of this instrument.

Over the past decade, the quality and quantity of solar observations from space- as well as ground-based observatories have improved dramatically. These observations have produced much detailed knowledge of structure and evolution of the solar atmosphere both in magnetically active as well as quiet period. At the same time a great progress has been made in theory to understand the physical processes that take place in the sun's interior and the solar atmosphere.

Scientifically rich observations of the solar atmosphere have become possible due to the enormous progress in the imaging systems and high-end spectroscopic instruments. There is a huge demand for the solar data with high temporal, spatial and spectral resolution taken in various wavelengths. Moreover, researchers often require observations of different layers of the solar atmosphere near simultaneously.

It is well understood that features in the solar atmosphere change very rapidly. The speed of evolution of these features increase with decreasing size. Hence, high spatial resolution observations always demand high temporal cadence. At high spatial resolution, these features usually evolve at the rate of sound speed. The chromospheric features, for example, are believed to change at much faster rate than the features at the photosphere. This can be attributed purely to the faster sound speed at the chromosphere compared to the photosphere. Also, within the limited exposure time enough photons need to be collected for good signal-to-noise estimates of the physical parameters. The collection of a large amount of photons can be achieved by using a large aperture solar telescope. But the spatial resolution is usually limited by the Earth's atmospheric seeing. By using the high-order adaptive optics and/or post-facto techniques, one can minimize the atmospheric seeing effects to achieve high spatial resolution imaging within a limited field-of-view (FOV).

It is well known that during active phenomena on the sun, there is a rapid change in the magnetic field, velocity field and intensity (at a rate faster than 1 sec) at various heights in the solar atmosphere (photosphere to corona). To observe the solar atmosphere at various heights simultaneously, it is necessary to image the sun at different wavelengths since each spectral line forms at different temperature and pressure (e.g., Ca II H and K 3968 and 3933 Å in the lower chromosphere, H $_{\alpha}$ 6563 Å in the chromosphere and He I 10830 Å in the upper chromosphere). It is not enough to do only the photometry of the solar atmosphere. In many occasions, it is more meaningful to have Doppler velocity and polarization measurements by scanning the spectral line profiles at different wavelength positions. This is only possible either using a high resolution spectrograph or very narrow-band imaging system (like a Lyot filter or FP based system). A basic requirement of such an instrument is the wavelength coverage (preferably from 4000 Å to 1.5 μ m), together with high wavelength stability (10 mÅ /hr) and

reproducibility of the selected spectral points over the observing period. The stated objectives can be achieved with a narrow band imaging system capable of high temporal cadence and fast imaging performance (3 or more image frames/sec), large spectral (200000-250000) and spatial (0.1 arcsec) resolution without compromising the large FOV (1.5 arcmin) of the target object.

3 Anticipated Science Goals

Several scientific problems require high spatial, spectral and temporal resolution data of the solar atmosphere observed at several spectral lines over a long time basis. In the following, we briefly describe various scientific problems that require high quality narrow band imaging data on a regular basis.

1. Shear in the active region magnetic fields at various heights in the solar atmosphere and its role in triggering the solar flares and coronal mass ejections.
2. Propagation of Alfvén waves and acoustic waves in the solar chromosphere under high spatial and spectral resolution.
3. Evolution of magnetic fields in the photosphere and chromosphere during filament eruption.
4. Evolution of magnetic fields in the emerging active regions.
5. Flare induced changes in the spectral line properties.
6. On the relationship between the velocity and magnetic fields in the magnetic structures.

In addition to the above suggested problems, the filter-based, high spectral, spatial and temporal resolution can also help us to address the broader issues like: (1) the region of magnetic flux cancellations in the solar atmosphere and (2) the question of when, where and why do we observe the small scale jet-like features in the penumbral chromosphere and so on.

4 Instrument Requirement

In order to study and examine problems suggested above it is extremely important to build narrow band imaging systems. The narrow band imaging system should be capable of fast scanning at finer spectral resolution without significant loss in the spatial resolution. Some of the commonly used methods for narrow band imaging are:

- Spectrograph and spectral scanning method.
- Lyot Filter (using a set of wave plates and polarizers).
- Michelson Interferometer.
- Fabry-Perot Interferometer.

The relative merits and drawbacks of the narrow band imaging systems suggested above are as follows:

- The spectrograph based instruments offer very high spectral resolution but suffer from the low temporal cadence due to long scanning time requirement of the required FOV (typically takes 1 hr to scan a large active region). Moreover the FOV is limited by the length and scan range of the spectrograph slit.
- The Lyot filters are good for narrow band imaging but the light throughput is very low (a few %) and hence need long exposures.
- Michelson interferometer is good, but the achieved spectral resolution is very low. Also, it cannot be used for a large wavelength range and cannot shift to different wavelength using a single interferometer. So, one need to build different Michelson interferometer for a different wavelength range.
- Fabry Perot (FP), as a single instrument may not be very useful for narrow band imaging. But it gives a very good spectral resolution when used in tandem.

The rasterization of the spectrograph to make the image can be avoided in the FP based narrow band imaging. But at the same time it needs a sequential tuning to scan the line profile. Since the light throughput is very high for the FP based system, the sequential scanning on the line profile can be done very rapidly (typically of the order of few seconds). This scanning speed may not be sufficient during flares as the line profile itself can change within few seconds. As a result, the dopplergrams and magnetograms obtained during the flares may not be very reliable. Despite this apparent drawback, the information about the line profile change itself is useful and hence it is still worth using. One of the major advantages of using scanning FP is that it can be switched between wavelengths very fast. So, by combining the FP with different set of filters it is possible to obtain the images in different wavelengths. This is one of our goals as described in Section 3. Given these relative merits and limitations of these different types of instruments, FP based spectrograph is chosen to achieve all the scientific goals presented in Section 3.

5 Fabry Perot Interferometer

A Fabry-Perot (FP) interferometer is a device which consists of two highly reflecting parallel plates. It selectively transmits a particular wavelength of light (when it is combined with the order sorting filter) corresponding to the resonance of the etalon.

In solar astronomy the narrow band imaging instruments are constructed by combining the FP with the birefringent filters; And also by using 2 or 3 FP in series in combination with the interference filter as an order sorter to form a multi-etalon system, it can be used as bi-dimensional imaging spectrometer (Kentischer *et al.* 1998; Cavallini, 2006).

The transmitted beam from the Fabry-Perot etalon is a fringe pattern. The intensity distribution of the transmitted beam is given by the Airy's formula (Jenkins and White, 1937),

$$I = \frac{I_{max}}{1 + F \sin^2(\delta/2)}, \quad (1)$$

where $I_{max} = A^2 T^2 / (1 - R^2)$ is the maximum value of the intensity. $F = 4R / (1 - R)^2$ is the reflective finesse. A, T and R are the amplitude of the incident light, transmittivity of the Fabry Perot etalon and reflectivity of the etalon surface respectively. δ is the phase difference between the transmitted rays and is given by,

$$\delta = (2\mu d \cos\theta) 2\pi / \lambda, \quad (2)$$

where μ is the refractive index of the media between the plates and λ is wavelength of the incident ray, d is the distance between the plates and θ is the angle of the incident ray with the normal. So, one can vary the phase between the successive transmitted rays by changing the refractive index of the material between the plates or by changing the distance between the plates or by changing the inclination of the FP surface or the angle of incidence of the rays. In other words, the wavelength scanning on the spectral line profile can be done with one of the above methods. But in practice it is easy to vary the phase difference by moving one of the plates or by varying the refractive index of the media between the plates. The transmitted beam is a periodic fringes with a maximum intensity of I_{max} and the minimum intensity is $I_{min} = A^2 T^2 / (1 + R)^2$.

The performance of the FP is characterized by two parameters: (a) the finesse and (b) the free spectral range. The finesse relates to the sharpness of the fringes. Apart from the reflectance, there are other parameters that also reduce the finesse and some of these are 'flatness of the plates' and 'parallelism of the plates' etc.

The wavelength spacing between two adjacent maxima in the channel that can be determined without ambiguity is called the 'free spectral range (FSR)' and is given by

$$FSR = \frac{\lambda^2}{2\mu d \cos\theta}. \quad (3)$$

So, the FSR decreases with increase in spacing between the plates.

For solar observation in the desired wavelength band, the FSR should be larger than the closely spaced spectral lines so that there will not be any overlapping of the other line while scanning.

The passband of the FP can be estimated from the FSR and finesse that are related as $\Delta\lambda = FSR / F = \lambda^2 / \mu d \sqrt{F}$. By decreasing the spacing between the plates the FWHM of the transmitted ray will increase. In a single etalon system the spectral resolution depends on the finesse of the etalon and is given by,

$$\frac{\lambda}{\Delta\lambda} \sim \frac{F2d}{\lambda}. \quad (4)$$

The detailed results of how the effective finesse changes with the wavelength, how the wavelength varies as the distance between the plates changes, the relationship between the spectral resolution and wavelength are given in Appendix A.

5.1 Types of FPI

Table 1: Comparison between different types of Fabry-Perot Interferometers.

	Air-gap FPI	Solid-gap FPI	Liquid-gap FPI
Refractive index	1.	2.3	1.3 - 2.11
FWHM (min.)	$\sim 20 \text{ m}\text{\AA}$	$\sim 100 \text{ m}\text{\AA}$	-
Total light throughput	$\sim 50\%$	$\sim 50\%$	-
FOV variation	$\Delta\lambda/\lambda \sim \theta^2$	$\Delta\lambda/\lambda \sim \theta^2/\mu^2$	$\Delta\lambda/\lambda \sim \theta^2/\mu^2$
Tuning device	Piezoelectric	Lithium Niobate	Liquid
Electronic requirement	Capacitance $\pm 600 \text{ V}$	Voltage regulator $\pm 3000 \text{ V}$	- -
Lifetime factors	Dielectric coatings	Material breakdown	leakage
Maintainance requirement	Parallelism	Parallelism	- -
Technology	Large etalons Ghost reflections	Thin elements super-polishing	- -
Disadvantage	Large etalons Local Finesse variations -	Wavefront error minimum etalon thickness High voltages	- - -
Advantage	Simplicity Technology is known	Larger FOV than air-gap FP Technology is not well known	Large FOV not well known

Historically, two types of Fabry-Perot interferometers (FPIs) have been used in solar observatories around the world. These are (1) air gap FP and (2) solid gap FP. Recently, another type of FP i.e., liquid gap FP has been introduced into the market. The defining features of different types of FPIs are described in Table 1 (cf. Gary, Balasubramaniam and Sigwarth, 2002). Many details in the Table 1 are self explanatory. With the current technology, it is possible to fabricate a large FP of diameter about 20 cm. Maintaining the plate parallelism is still a technically challenging task. Also, a prefilter of that big size (about 20 cm) is not readily available in the market. Large air-gap based etalons need large optics and more space.

In the case of solid etalons the wafer should be thin and it should be well polished with surface accuracy of $\lambda/200$ or better. The solid gap based etalon offers a large FOV for the same size of air-gap based etalons. A very thin wafer is extremely fragile and may require several careful trials to make one. Only a very few companies have the expertise to make the solid-gap based etalons. Due to large refractive index of the material, any surface imperfection in the wafer will lead to larger error in the wavefront. In changing the refractive index in the solid state etalons it is necessary to use a high voltages. Even though it may not be a problem to build a high voltage power supply, the substrate could easily breakdown at very high voltages. Moreover, the solid etalon are very sensitive to ambient temperature changes. Therefore, an accurate temperature control is extremely necessary to ensure the desired performance. In comparison to solid etalon, the air-gap based etalons are less complex and easy to handle in day to day operation.

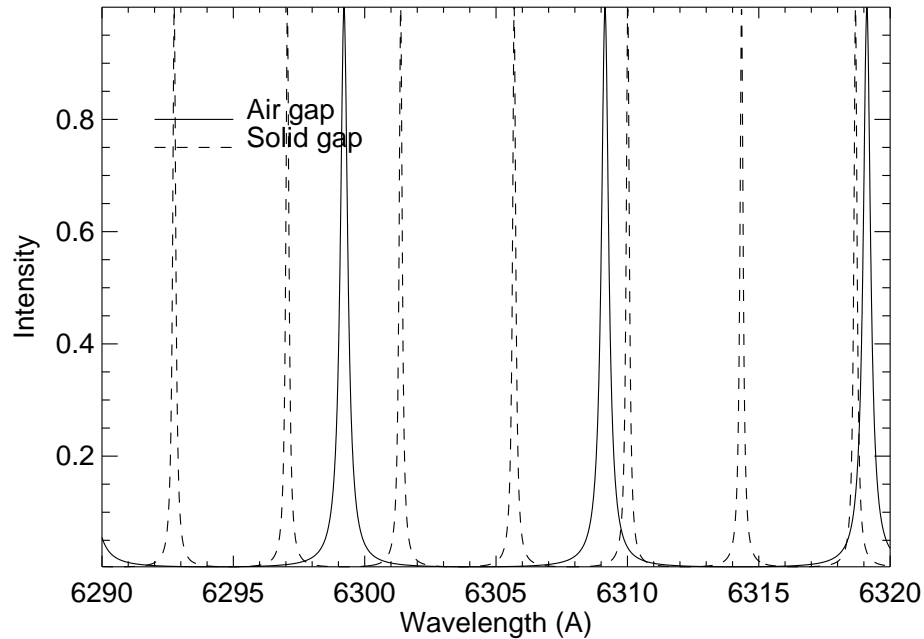


Figure 1: The transmission profile of the air gap (solid line) and solid gap (dashed line) based interferometer. The intensity is normalized to unity.

The transmission profile of the air gap and solid gap based FP is shown in Figure 1. From Table 1 and Figure 1, it is clear that the air-gap based etalon has many advantages compared to the solid gap: (i) FSR is larger hence order sorting filter can have broader FWHM, (ii) Smaller voltage requirement to drive the electronics and (iii) Large finesse. In the solid gap etalons, Because of complex process involved in polishing the wafer it is very difficult to produce etalons with an effective finesse larger than 25. The high refractive index (~ 2.3) of the solid wafer (crystal) increase the surface irregularities

and the crystal should be polished at least 5 times better than the surface accuracy of the glass substrates used in the air-gap etalons. The disadvantages of smaller FOV compared to the solid-FP will be overcome by having a large aperture air-gapped FPI. With the advanced technology of piezoelectric feedback drivers it is possible now to maintain the parallelism with an accuracy of better than $\lambda/10000$ in air-gap FP. The wavefront errors, super-polishing of the Lithium-Niobate and the induced polarization by the crystal are unknown yet in solid-gap FP. Even we do not know how much is the variation in the refractive index of the material for different temperature. Also, once the solid etalons are made available it is impossible to change its plate separation and it is very important to reduce the parasitic light (see Section 5.5). In case of air-based etalons, one can change the nominal plate separation if needed. Because of the operational complexity and uncertainties of the solid etalons, we prefer to use the air gap etalons in our design.

5.2 Fabry-Perot Optical Mounting

There are mainly two common ways to mount the Fabry-Perot interferometer (FPI) in the optical path. These are: (1) collimated mounting and (2) telecentric mounting.

Collimated mounting:

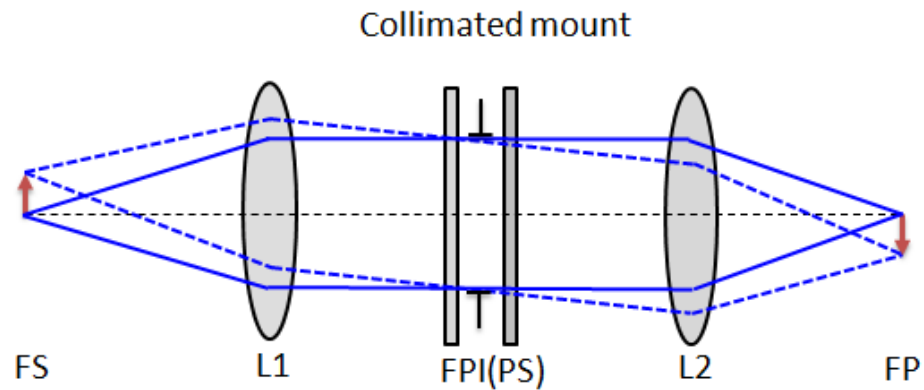


Figure 2: An optical layout for the FPI system in collimated beam (Kentischer et al. 1998). The lens L1 images the telescope aperture into the FPI. The re-imaging lens L2 forms the image on to the CCD camera through the FPI.

Figure 2 shows the FPI in collimated configuration. In this configuration the FPI is kept in the collimated beam. In other words, the FPI is positioned close to the image of the telescope's entrance pupil. Hence, every point on the image will subtend certain angle with respect to the optical axis of the FPI and hence different plate separations for each image point. This leads to a wavelength shift across the FOV of interest. In other words wavelength of the transmitted light at the edges of the FOV is blue shifted.

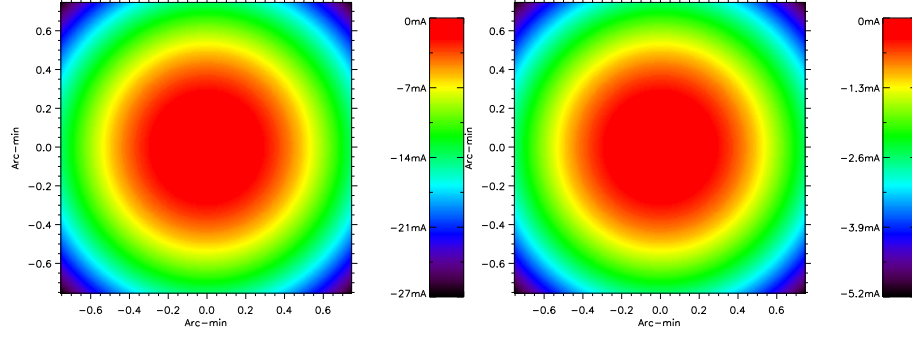


Figure 3: Left: Wavelength gradient developed across the FOV in air-gap FPI. Right: same as left side image but for solid-gap FPI.

Also in this configuration, any non-uniformity or parallelism errors will lead to spectral broadening since the beams are collimated going through the FPI.

The shift in the wavelength due to the angle of incidence is given by,

$$\Delta\lambda = \frac{\lambda}{2} \left(\frac{\theta}{\mu} \right)^2 \quad (5)$$

where θ is the maximum angle of incidence and is given by,

$$\theta = FOV_{1/2} \frac{A_{telescope}}{A_{fp}} \quad (6)$$

$FOV_{1/2}$ is half diagonal FOV, $A_{telescope}$ is the aperture of the telescope and A_{fp} is the aperture of the FP. For FP with an aperture of 15 cm with an air gap ($\mu = 1$), telescope with a size of 2 m, a FOV of 1.5 arcmin and observation done at a wavelength of 6300 Å, a shift in the wavelength is about 27 mÅ (Figure 3, left). The wavelength gradient developed in the solid gap ($\mu = 2.3$) is very small compared to the air gap based FP for the same FOV (Figure 3, right). This is purely due to their refractive index which is larger in solid-gap than in the air-gap FPI.

Telecentric Configuration:

In telecentric configuration (Figure 4), the FPI is placed in an intermediate image plane and the pupil image is collimated. In this configuration, there is no systematic wavelength shift over the FOV due to the reason that each point on the final image passes through the full cone angle at the FPI. The maximum allowable beam angle within this cone is a function of the f -number of the telecentric beam. In order to obtain the desired spectral resolution, the angle of the cone should be minimized. In fact, the telecentric mode allows one to trade spectral resolution against FOV. Table 2 summarizes the merits and demerits of these two configurations. In spite of this, the cone angle can produce broadening of the effective passband and is given by,

$$FWHM_{eff} = (FWHM^2 + \Delta\lambda_s^2)^{1/2}, \quad (7)$$

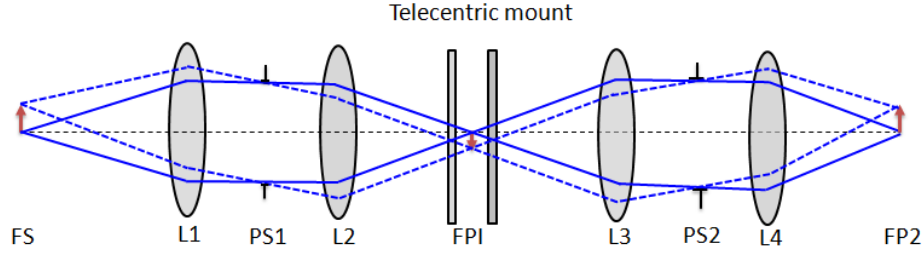


Figure 4: An optical layout for the FPI system in telecentric beam (Kentischer et al. 1998). The solar image (FS) with 90 arcsec FOV is projected into the FPI system using L1 & L2. L3 & L4 re-image the FOV onto the detector (FP2). PS1 and PS2 restricts the beam size.

Table 2: Comparison between the collimated and telecentric optical configurations of FPIs.

	Collimated	Telecentric
Wavelength shift across the FOV	yes	no
Wavefront distortion	large	small
Influence of dust on the image	low	large
Alignment sensitivity	large	low
Blocking ghost reflections	difficult	easy
Influence of plate shape	broadening	wavelength shift
Spectral line broadening	No	Yes

where, $FWHM$ is the full width at half maximum of the FP and $\Delta\lambda_s$ is the wavelength shift across the FOV. For example, to achieve a spectral resolution of 200000 (an effective broadening of 32 mÅ at 6302Å) using 15 cm aperture FP, 1.5 arcmin FOV, the FWHM of the FP should be less than 18 mÅ. With the same setup for a solid-gap FP with refractive index of 2.3, the required FWHM will be close to 30 mÅ. So, there is very little broadening of the spectral line in the solid-gap compared to the air-gap based FPIs.

5.3 Instrument Design Specifications

The FP etalons in series has better performance than just a single FP. For our purpose we would like to have: (1) high spectral resolution, (2) large spectral range, (3) large field-of-view to cover the sunspot as a whole, (4) high light throughput to have sufficient light, (5) fast change between wavelengths, (6) good wavelength stability, and (7) minimum stray light. Table 3 shows the required parameters to achieve the different science goals as presented in Section 3.. Table 4 gives the design specifications of the FP based imaging spectrometer that can meet our scientific goals.

Table 3: The requirements to achieve the proposed science goals are listed here. In the Table SG, SL, IC, RQ, RES, FOV, AR and CAD corresponds to science goals, spectral line, image cadence, requirement, spatial resolution, field-of-view, additional requirement and the cadence required for the additional requirement respectively. And Dop, VMG, SPL, LM and Int corresponds to Dopplergram, Vector Magnetogram, Spectral line, line-of-sight magnetogram and intensity image respectively. The science goals are written in a sequence as described in Section 3.

SG	SL	IC	RQ	RES	FOV	AR	CAD
1.	H α 8542	30-40 s	Int	0.1''	1.5'	VMG	2 min
2.	8542 Dop	1 Frame/s 2/min	Int	0.1'' 0.1''	1-1.5'	VMG	20 min
3.	8542	2 min	Int Dop	LM	60''	VMG	20 min
4.	8542	1-min	LM DOP	0.1''	20-30''	VMG	10-20 min
5.	6302	1 sec 20 sec 20 sec	SPL LM DOP	0.1'' 0.1'' 0.1''	10-20''		
6.	6302 8542 5576	1 min 1 min 1 min	0.1'' VMG 0.1'' VMG 0.1'' Velocity	0.1'' to 1.0''	30'' to 90''	Int	10 sec

Table 4: The design specifications of the narrow band imaging system with 2 FP in series.

Spectral Resolution	≥ 200000 at 6000\AA
Spectral Range	$5000\text{\AA} - 9000\text{\AA}$.
Field of View	≤ 1.5 arcmin
Maximum Ghost Transmission	10^{-4}
Signal to Noise Ratio	≥ 500
Peak Transmission	$\geq 50\%$
Wavelength Stability	$\leq 10\text{ m\AA/hr}$
Tuning Rate	$\geq 10\text{ pm/ms}$
Blocking Prefilter	$2-3\text{\AA}$ range
Maximum Stray Light	10^{-3}
Image Cadence	≥ 1 frame per sec

5.4 Optical Configurations of the FP Based Spectrometer

Figure 5 shows a typical optical layout for the dual FP in a telecentric configuration. A set of collimator lens and imaging lens before the FPs form an intermediate image near the first FP and then another set of collimator and re-imaging lens forms the final image on the CCD camera. A prefilter with a 3\AA passband can be used in between the FPs

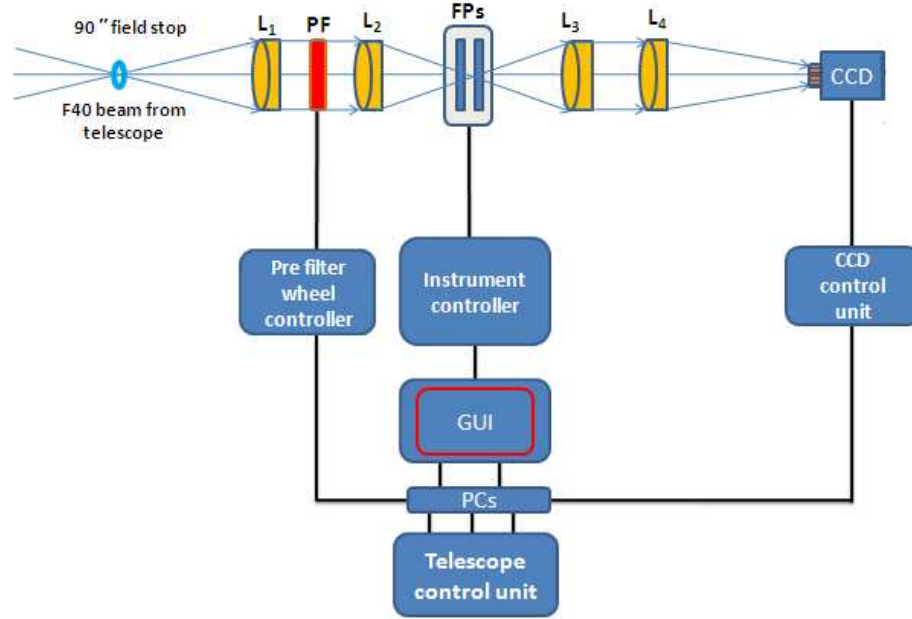


Figure 5: Schematic layout of the optical elements for a dual Fabry-Perot etalons in tandem.

or in the collimated beam. If we keep the prefilter in between the FPs it will reduce the ghost reflections between the FPs (Cavallini, 2006). On the other hand by keeping the prefilter in the collimated beam will reduce the size of the prefilter. Small size filters ($\sim 5\text{-}6\text{ cm}$) are readily available in the market. A CCD camera with a required area for the chosen FOV will be kept at the final image plane. The prefilter assembly can be kept inside the temperature controlled oven with motorized control to change different filters.

The field stop restricts the FOV and it also prevents the scattered light from entering into the FP optical system. A beam splitter placed after the field stop (not shown in Figure 5) is used to tap a small amount of beam (may be $< 10\%$ of the main beam) to form continuum images. These continuum images are useful for doing post-processing on the images (like destretching, co-alignment of various images taken in different wavelengths etc).

Since the system is dual FP in series, there will be ghost images formed by the reflection between the two FPs. The intensity of the ghost images is about 12% of the transmitted beam for the first reflection and 5% of the transmitted beam for the second reflection. The ghost can be removed by tilting the FPs by a small angle of 0.1° or by placing the order sorting filter in-between the two FPs. Even though the tilt removes the ghost but it introduces intensity gradients in the transmitted beam due to the shift in the passband of two FPs.

The whole system including the CCD camera needs to be automated. The automa-

tion software should do the following: (1) maintain the parallelism of the two plates in FPs, (2) lock both the FPs on the desired solar line, (3) scanning over the line profile, (4) centering of the prefilter passband, (5) synchronization between the CCD and FP scanning, and (6) take the flat field on various wavelength over the line profile. A graphical user interface (GUI) will be required to communicate between the computer and the observer. Most of the tasks for the etalon shall work automatically and they should be synchronized with the temperature controller, CCD camera and the prefilter assembly. And finally - at the later stage - the whole setup can be made controllable remotely.

5.5 Fabry-Perot Etalons in Combination With the Order Sorting Filter

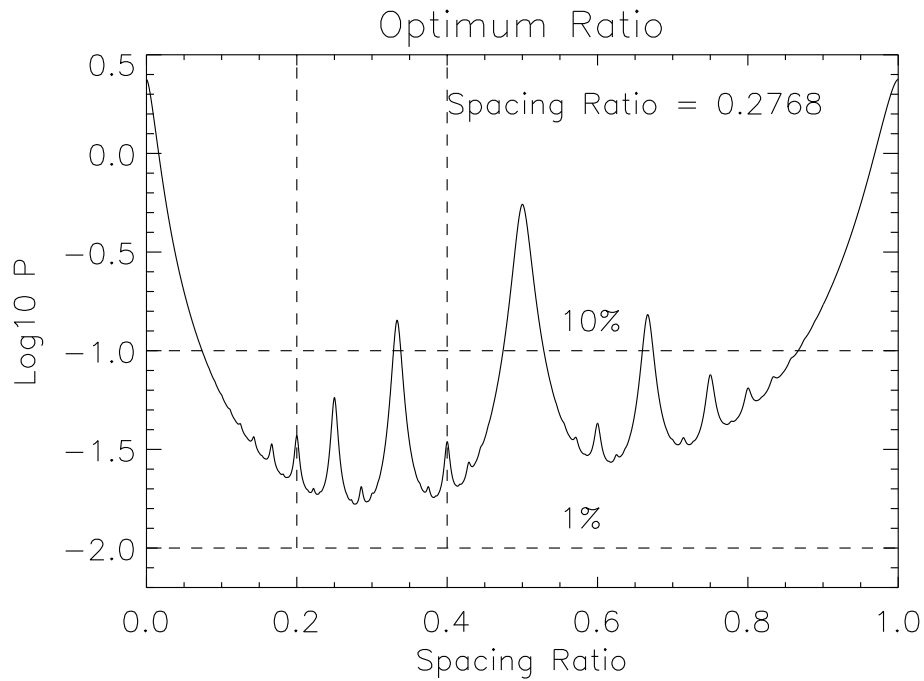


Figure 6: A plot of parasitic light vs spacing ratio for dual-etalon system. The two vertical lines define a range where the contribution from the parasitic light is the minimum. The two horizontal lines indicate the 10% and 1% level of the parasitic light.

In the proposed narrow band imager (Section 5.4) there are two FPs kept in tandem with the narrow band order sorting interference filter. If N such FPs are kept in series with the order sorting filter then the resulting instrumental profile $I(\lambda)$ is obtained by,

$$I(\lambda) = I_{IF}(\lambda) \prod_{i=1}^N I_i(\lambda). \quad (8)$$

where, I_{IF} is the transmission of the order sorting filter, and i varies from 1 to N . The advantages of using more FPs are: (1) the unwanted side interference orders are suppressed, (2) the spectral resolving power increases, and (3) the interference filter (IF) with larger passband can be used. Some of the disadvantages are: (1) increase in system complexity, (2) the overall decrease in transparency, and (3) the loss in optical quality. The main goal of our project is to achieve a high spatial and spectral resolution without losing the optical quality. Hence, we preferred a dual etalon system rather than triple or more.

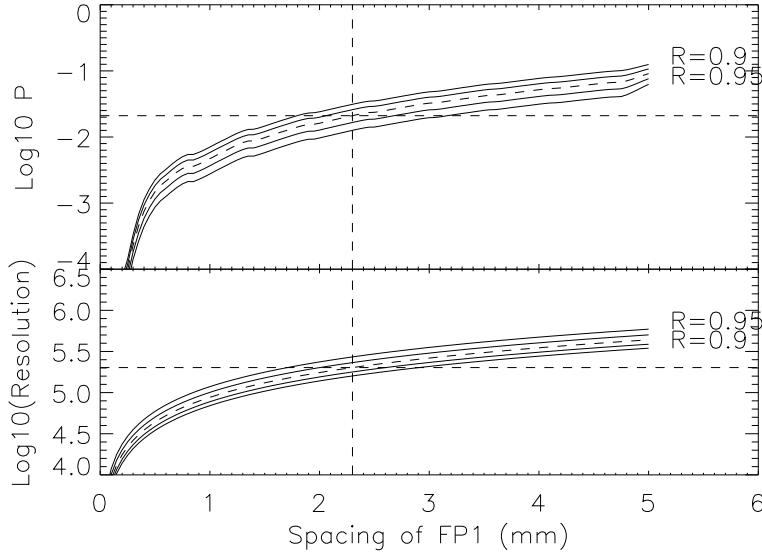


Figure 7: Top: A plot of parasitic light (P) at 6300 \AA vs the spacing of the thickest FPI is shown. Bottom: Spectral resolving power (R) at 8600 \AA is plotted as a function of spacing of the thickest FPI. These plots are shown for reflectivity of 0.9 to 0.95 in steps of 0.01. The middle dashed line refers to a reflectivity of 0.93.

Once the number of etalons and the mounting system have been defined, the next step is to search for the optimum ratio between the interferometer spacings at which it best reduces the parasitic light from the side bands. The parasitic light is defined as the ratio between the flux outside and inside the instrumental profile. By using the methodology given in Cavallini (2003) we estimated the parasitic light with the following parameters: the refractive index $\mu=1$, the incidence angle $\theta=0$, absorption coefficient $A = 0.01$, coating reflectivity $R = 0.95$, $\text{FWHM}_{IF} = 3 \text{ \AA}$ centered at 6302 \AA , and peak transparency $\tau_{IF}=0.3$. Figure 6 shows the plot of parasitic light vs the ratio of the FPIs spacing. Here we have kept the first FPI (FPI-I) at 2 mm and varied the spacing

of the second FPI (FPI-II) insteps of 0.01, till the ratio equal to 1 (ratio = d_2/d_1 where d_1 & d_2 are the separation between the plates in FPI-I and FPI-II).

From the plot (Figure 6) it is clear that the smallest level of the parasitic light is obtained for the spacing ratio of 0.277. The estimated parasitic light is for 6302 Å wavelength. This being the optimum ratio, now one can adjust the spacing between the plates of FP-I such that the spectral resolution is optimized. Again by following the method of Cavallini (2003) we optimize the spectral resolution $R = 2.0 \times 10^5$ (Figure 7, bottom) for a spacing of FPI-I = 2.283 mm at which the parasitic light is less than 2% (Figure 7, top). So, the dual FPs with a spacing of FPI-I 2.283 mm and FPI-II 0.637 mm and a coating reflectivity $R = 0.93$ have been considered as the best values for getting the best parameters such as large transparency, low ghosts, low parasitic light, high image quality and high spectral resolution.

5.6 Minimum Size of the Required Fabry-Perot

The spectral resolution in the telecentric mounting depends on the focal ratio of the beam. In the collimated beam the FWHM of the transmitted spectral line can be approximated as,

$$\Delta\lambda_{FWHM} \sim \frac{\lambda_0^2}{\pi d_1 \sqrt{F(1+\epsilon^2)}}. \quad (9)$$

where, λ_0 is the central wavelength, d_1 is the spacing of the FPI-I in the series and $\epsilon = d_2/d_1$. In this calculation, $d_1 = 2.3$ mm (obtained from Section 5.5) and $\epsilon = 0.277$. At the 6302 Å line, the FWHM ($\Delta\lambda_{FWHM}$) is estimated as 19.2 mÅ.

In the telecentric configuration, the collimated FWHM ($\Delta\lambda_{FWHM}$) adds with the telecentric spread $\Delta\lambda_s$ as follows:

$$\Delta\lambda = \sqrt{\Delta\lambda_{FWHM}^2 + \Delta\lambda_s^2}. \quad (10)$$

With the requirement that $\Delta\lambda$ equal to 33mÅ we get a telecentric spread $\Delta\lambda_s = 27$ mÅ. The change in the FWHM as a function of half angle α of the telecentric ray cone is approximated as,

$$\Delta\lambda_s = \frac{\lambda_0}{8F_{no}^2}. \quad (11)$$

where, the F_{no} is the focal ratio of the telecentric beam. For 6302 Å line, the estimated focal ratio is 170.8.

Following Darvann and Owner-Petersen (1994), the required size of the FP for a given FOV is given by,

$$D_{FPI} = F_{no} \alpha_{FOV} D. \quad (12)$$

where, the α_{FOV} is the FOV and D is the diameter of the telescope. For a telescope of 2 m class and a FOV of 1.5 arc-min, the clear aperture of the FP should be 14.9 cm. Hence, the adoption of 15 cm aperture air gap FP from IC Optical Systems Ltd. (UK) or any other company can be utilized for this project. At this focal ratio the spectral

resolution at 6302 \AA is 1.91×10^5 which is close to the desired parameter in the design specification that meets all our scientific goals.

5.7 The Transmission Profile of the Air Gap FPI system

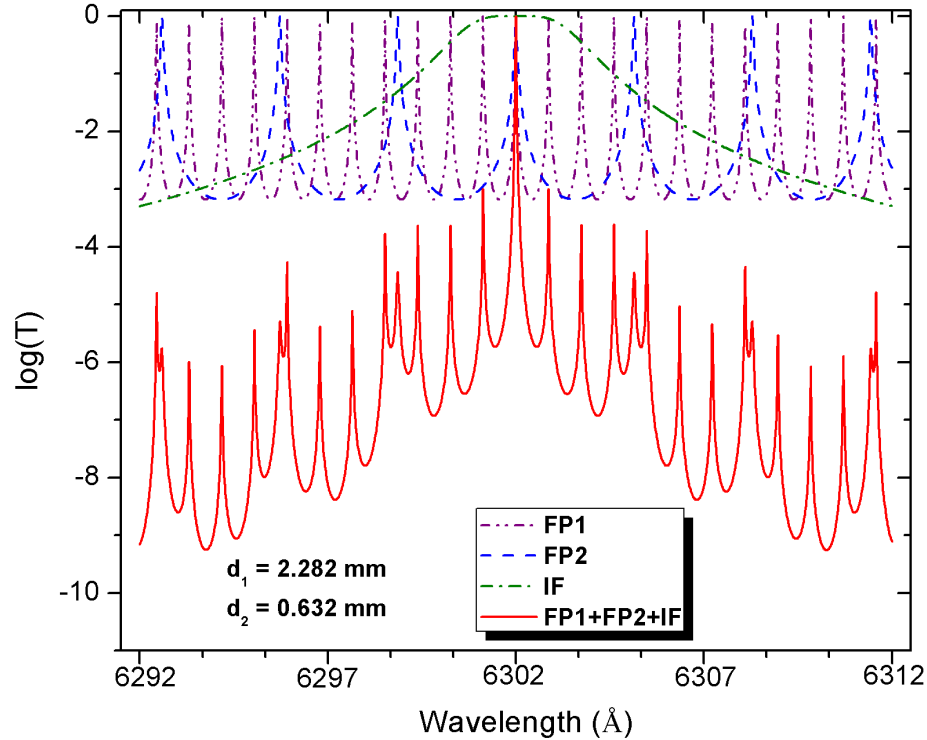


Figure 8: The transmission profile of the dual air-gap FPIs in combination with a 3 \AA transmission filter. The reflectivity of 0.93 is taken in computing the transmission profile.

Figure 8 shows the transmission profile of the air gap media of dual FPIs in tandem. In estimating the transmission profile of the dual FPI system we have used the spacing of the FPI-I as 2.283 mm and the FPI-II as 0.632 mm, with a reflectivity of 0.93 and the FWHM of the transmission filter as 3 \AA with two cavities. The profile shown here is for the FPIs kept in the collimated beam. In the telecentric configuration, the transmission profiles will be similar except that the spectral line will be broadened due to the large FOV.

5.8 Specifications of the Fabry-Perot Etalons

The IC OpticsTM makes piezoelectrically tunable etalons that are constructed using two highly polished glass plates. One of the glass plates is mounted on the movable piezoelectric stacks. The IC Optics FP operates on the three channel bridge system using capacitance micrometers and piezoelectric actuators. A combination of capacitance micrometer and piezoelectric actuators monitor and correct the errors in mirror parallelism and spacing. Out of three channels, two channels control parallelism and the third maintains the plate spacing by locking it to the cavity length. This is achieved by referencing the capacitor to a high stability standard reference capacitor. The whole unit functions in a closed loop servo system, thus eliminating any nonlinearity and hysteresis in the piezo drive. The detailed specifications of the required FP is given in Table 5.

Table 5: Details of the required specifications of the FPs for narrow band imaging system.

Specification	Value
Fabry Perot Substrate Material	Fused Silica
Reflectivity	0.95 at λ 6000-9000 Å
Type of FP	ET 150 IC Optics Inc.
Clear Aperture	15 cm
Surface Accuracy	$\lambda/200$
Number of FPs	2
Etalons Plate spacing	2.283 mm for FP-I and 0.637 mm for FP-II
Coating	Multilayer Coating
Displacement	$\pm 2\mu\text{m}$ with 4096 steps

5.9 Stability of the Spectrometer Over the Wavelength

The FP based spectrometer are usually kept inside a temperature controlled enclosure with the ambient temperature specified by the manufacturer. The temperature should be maintained constant within 0.1°C or better depending on the manufacturers specification of the FP. Temperature controller is calibrated based on the careful laboratory measurements of the wavelength drift with temperature.

Wavelength stability of the FP system is generally calculated from the accuracy of the temperature controller, tolerance to the parallelism of the plates, beam angle with respect to the plates and plate separation etc. Typically the required stability of the wavelength is about 10 mÅ /hr, which is much smaller than the resolution of the spectrometer.

5.10 The Exposure Time and Signal to Noise Ratio

It is very important to know the exposure time and the signal to noise ratio (SNR) at the detector. These quantities can be calculated by using the reflectance and transmittance

of all the optical components in the path of the beam. The solar flux at 6318 Å continuum wavelength (which is close to 6302 Å) is $1.638 \times 10^9 \text{ J m}^{-2} \text{ m}^{-1} \text{ s}^{-1}$ ($1.638 \text{ W m}^{-2} \text{ nm}^{-1}$) (obtained from <http://lasp.colorado.edu/sorce/index.htm>) which corresponds to a photon flux of $5.201 \times 10^{27} \text{ photons m}^{-2} \text{ m}^{-1} \text{ s}^{-1}$. We can relate the photon flux to the number of electrons at the detector per second assuming the specific characteristics of the telescope and the imaging instrument. We assume the atmospheric transmission is $\tau_{atm}=0.95$. This is almost close to the quoted value of atmospheric transmission if one neglects molecular scattering and aerosol absorption (Cox, 2000). The proposed NLST telescope will have a six mirrors (including the primary) each with a reflectivity of 95%. The intensity of the reflected beam from the primary of the telescope to the end of sixth reflecting surface is reduced to $\sim 70\%$ which takes the atmospheric transmission into account. The lens-let array of the adaptive optics system will take-out a few percent of the beam and other instrument will require a few more percent of the main beam. Hence, while reaching the proposed narrow band imaging system the intensity of the beam will be reduced to 60%. The transmission of the etalon is 80% each and the order sorting filter transmits the light by about 40%. Hence, the final beam will have an intensity of 15% of the original solar flux. The FWHM of the imaging instrument is 33 mÅ. The FOV is 1.5 arcmin circular. For a 2048×2048 pixel CCD camera (pixel resolution of 0.06 arcsec) with 60% quantum efficiency we should be able to detect $6.43 \times 10^6 \text{ electrons s}^{-1}$ which corresponds to an exposure time of about 54 ms for a full well of $3.5 \times 10^5 \text{ electrons}$. To avoid the image saturation, it is sufficient to consider about 80% of the full well capacity with 43 ms exposure time. If the CCD readout time is about 100 ms then we should be able to get at least 6 images per second. At this photon detection level the SNR is 532. So, for a 0.06 arcsec resolution there are enough photons to achieve the desired SNR. For a Nyquist sampling at the diffraction limit of the 2-m class telescope, (0.039 arcsec per pixel), a CCD larger than 2048×2048 pixels is necessary to cover the required FOV. The SNR of > 500 can be attained with an exposure time of 100 ms or larger. Even at this resolution, the cadence will be around 5-frames per second.

It is also possible to make the dopplergrams with this dual FPI system. By acquiring the intensity images in the red and blue wing(s) of the 6302 Å line (or any other line) one can make the dopplergrams. The intensity can be measured in the red and blue wing at a position of 60% level below the continuum. Then by using the simple relation, one can construct the Doppler maps as,

$$V_{dop} = K \frac{I_{red} - I_{blue}}{I_{red} + I_{blue}}. \quad (13)$$

The error in measuring the Doppler velocity for zero shift in the wavelength position is given by,

$$\sigma_v = K \sqrt{\frac{1}{I_{red} + I_{blue}}}. \quad (14)$$

The photon counts at the 60% intensity of the continuum will be $6.43 \times 10^6 \text{ photons s}^{-1}$. Using this value, the error in measuring the velocity can be estimated to be $2.795 \times 10^{-4} \sqrt{K}$. Here, the K is the calibration constant, measured in terms of km s^{-1} .

This constant will vary with different spectral lines. After using the 6302 Å line with a 40 mÅ FWHM (of the narrow band FPI system) the value of K is $7506.13 \text{ km s}^{-1}$. Using this value of K we estimated the error in the Doppler velocity to be about 24 m s^{-1} .

The estimation of the error in measuring the magnetic field using polarimetry will be discussed in a separate technical report.

6 Items Needed and Cost of the Project

Table 6: The required components for the project.

Items	Price
Fabry Perot Interferometer	$13000000 \times 2 = \text{Rs. } 260 \text{ lakh}$
Order sorting filters	$500000 \times 5 = \text{Rs. } 25 \text{ lakhs}$
CCD camera	40 lakhs
Lenses, prism, optical table & opto-mechanical mounts etc	30 lakhs
Temperature controlled enclosure and platform	5 lakh
Electronic and electrical items	10 lakhs
Enclosure, Filter Wheel & Miscellaneous	20 lakhs
Total	390 lakhs

Based on the above suggested optical layout for the FP based spectrometer (Figure 5) it is necessary to have a set of combination of lenses. The lenses will be achromatic doublet and will be able to cover a wavelength range of 5000-9000 Å. A 5-10% beam splitter is required to tap a portion of the main beam to be utilized for the continuum imaging purpose. It is also necessary to have a set of interference filters with a pass band of 2-3 Å for different wavelengths of interest. Few wavelengths of interest are: H_{α} 6563 Å, Fe I 6302 Å filter, and Ca II 8542 Å line.

It is also important to have a good performance CCD camera with the specifications mentioned in Section 5.10. Other accessories include mechanical components, holders, clamps, posts etc. Finally an optical table, a tunable laser or a spectrometer are necessary to calibrate the FPs in the laboratory and study its performance.

The cost of each item depends on the quality, quantity and the vendor who provides them. The most expensive item in this project is the FPs. The cost would include the interface card, control software, piezo-electric controller, power supply etc. The next expensive item is the prefilter assembly. The optical and mechanical items (CCD camera, vibration free table, temperature controller, optics etc) would also cost a significant amount. Based on the current estimates, the tentative budget of the entire project is around Rs. 400 lakhs. The material cost may change with time. A revised cost estimate would be made at the time of detailed project report.

7 Other Contemporary Instruments

Table 7: Comparison of FP based narrow band imaging system around the world. TESOS, IBIS, VTT and NLST corresponds to Telecentric Etalon SOLar Spectrometer, Interferometric Bidimensional Spectrometer, Vacuum Tower Telescope and National Large Solar Telescope respectively. In the Table, $\Delta\lambda$ corresponds to spectral resolution, Pixel Res corresponds to spatial resolution in terms of arcsec/pixel and FOV is the field-of-view.

System	$\Delta\lambda$	Pixel Res arcsec	FOV arcsec
TESOS	320000/160000	0.15	100
IBIS	200000	0.2	80
VTT	160000	0.11	78×58
NLST	200000	0.06 & 0.039	90

The Telecentric Etalon Solar Spectrometer (TESOS) is a triple etalon system, developed and installed at the Observatorio del Teide, Tenerife. The observation is done at 0.15 arcsec resolution and FOV is 100 arcsec. The system works in the optical wavelength region. The Interferometric Bidimensional Spectrometer (IBIS) was developed by the Italian group and installed at the Dunn Solar Telescope (DST) of the National Solar Observatory, USA. This is a dual etalon system with a spatial resolution of 0.2 arcsec and a FOV of 80 arcsec. The spectral resolution is 200000 and operating at near infra-red wavelength range. The Institut Für Astrophysik developed a 2D spectrometer for the VTT in 1986 and they have upgraded it in 2005. The FOV is 78 arcsec×58 arcsec, with a pixel resolution of 0.11 arcsec. This instrument works in the wavelength range of 5300-8600 Å with a spectral resolution of 160000.

Table 7 shows the comparison of all the instruments including the proposed narrow band imaging system for the NLST. In all these instruments, the spectral resolution and FOV is comparable to our proposed imaging system, except the spatial resolution which is large by a factor of 2 or more in our case. With this resolution we will be able to achieve the projected science goals. We will follow some of the concepts in the designs and characteristics of these instruments in our proposed instrument.

8 Summary

The Indian Institute of Astrophysics is planning to build a 2-m class telescope to be commissioned in one of the high altitude sites in Himalayas. This telescope will be dedicated to the solar astronomy to do the observations at high angular resolution. The current report describes an instrument for narrow band imaging with high spatial and spectral resolution. This report is written with a clear goal of deploying the FP based spectrometer on the NLST as one of the back-end instruments for solar observations. It is also assumed that the NLST project will have fully functioning adaptive optics system and also the post-processing capabilities like speckle, destretching etc. The projected FOV may not be available all the time at the full spatial resolution (due to the

seeing limitations and the limitation of the AO correction away from the iso-planatic patch) but it is sufficient to cover certain type of observations as mentioned in the scientific goals.

NLST is one of the high priority projects of IIA which is proposed to fulfill the long standing desire of the solar community in the country. The 2-m class high resolution telescope is expected to help address many intriguing problems in solar physics. The key scientific goals of the telescope are explained in the NLST project document (NLST proposal (2006)). As usual, the back-end instruments will play an important and decisive role in realizing the stated objectives of the project. To this end, we have proposed a narrow band dual Fabry-Perot imager to study the various aspects of solar atmosphere at different wavelengths. The proposed FP design is supported by detailed studies comprising stray light modeling, ghost transmission, optimum plate spacings, mounting configurations and computer simulations described in the preceding sections. These results clearly show that the designed instrument will be capable of achieving the desired spectral and temporal resolution necessary to meet the requirements of narrow band imaging system for NLST.

9 Acknowledgments

We would like to thank Drs. Sankarasubramanian, Shibu Mathew, Raja Raja Bayanna and Rangarajan who have helped us at various stages of this proposal. We also would like to thank Profs. Tushar Prabhu, Rangarajan and A.K Saxena for valuable comments.

Appendix

The effective finesse (Fi_{coll}) in the collimated beam is (Darvann and Owner-Petersen, 1994),

$$Fi_{coll} = \frac{\pi}{2} \left(\frac{1}{F} + \left(\pi \frac{\lambda_r}{\lambda_p} \frac{1}{q} \cos(\theta) \right)^2 \right)^{-1/2} \quad (15)$$

where, F is the reflective finesse, λ_p is the peak transmission wavelength, $1/q$ full width fractions of a reference wavelength λ_r . Hence, the finesse is a function of mounting and of surface flatness, parallelism, and reflectivity R . Figure 9 shows the variation in finesse as a function of wavelength. The plot is shown for two values of reflectivity 0.9 and 0.95. The surface flatness is taken to be $\lambda/150$ or better at 5000 \AA . The angle $\theta = 0$. From the plot it is clear that effective finesse decreases with decrease in reflectivity.

The spectral resolution of the FP system in the collimated beam is given by,

$$Res = 2Fi \frac{d_0 \cos(\theta)}{\lambda_p} \quad (16)$$

Figure 10 shows the plot of minimum spacing needed to obtain a resolution of 2×10^5 as a function of wavelength. The results are shown for two different reflectivities. It can be seen in the plot that the spacing between the plates increases as the

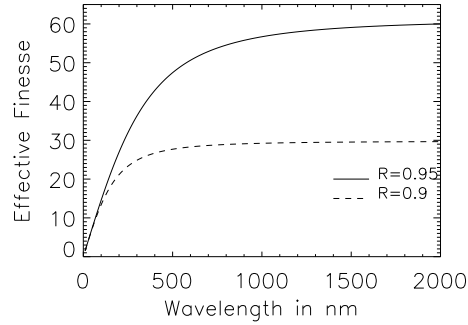


Figure 9: A plot of effective finesse as a function of wavelength is shown here. The solid curve is for the reflectance of 0.95 and the dashed curve is for the reflectance of 0.9.

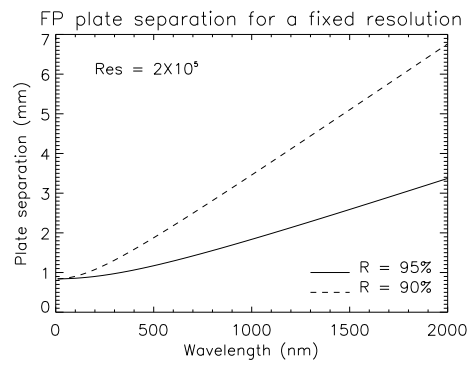


Figure 10: A plot of optimal spacing needed to obtain a resolution of 2×10^5 as a function of wavelength. The solid curve is for the reflectivity of 0.95 and the dashed curve is for the reflectivity of 0.9.

wavelength increases to keep the same resolution of 2×10^5 . And as the reflectivity increases the spacing required to keep the same resolution is small compared to the smaller reflectivity. But at the same time as the spacing increases, the FSR decreases resulting in larger ghosts in the image.

By assuming the reflectivity as 0.95, we have plotted the resolution as a function of wavelength for a fixed spacing between the FP plates (Figure 11). From the plot it is clear that the resolution decreases as the wavelength increases and the resolution is large for larger separation.

According to the manufacturer the spacing can be tuned within an error in the spacing of $3 \mu\text{m}$. For such an error in the spacing, the scanning range in the wavelength is given by,

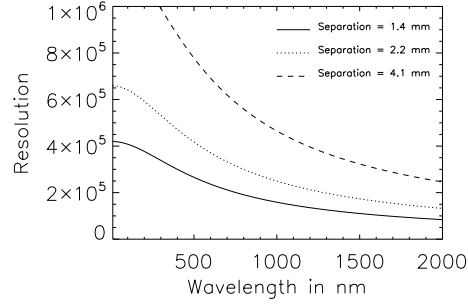


Figure 11: A plot of spectral resolution as a function of wavelength for a fixed plate spacing.

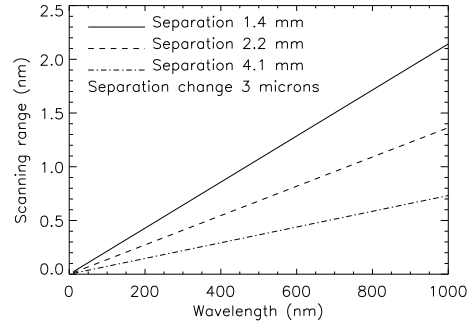


Figure 12: A plot of scanning wavelength range at different wavelengths for a fixed plate separation of 1.4, 2.2 and 4.1 mm with a $3\mu\text{m}$ error in spacing .

$$\Delta\lambda_p = \lambda_p \Delta d / d_0 \quad (17)$$

where, the Δd is the error in keeping the correct spacing d_0 . In our calculation $\Delta d = 3\mu\text{m}$ and d_0 is the spacing between the FP plates and it is fixed at 1.4 mm, 2.2 mm and 4.1 mm. Figure 12 shows the plot of scanning range in wavelength due to the error in the spacing distance of about $3\mu\text{m}$ as a function of wavelength. From the plot it is clear that the scanning range in the wavelength is large for longer wavelength. It is larger than 3 \AA for a plate separation of 2.2 mm at the wavelength of 6300 \AA . So, a separation of 4.1 mm or larger is required to keep the scanning range within 3 \AA . But at that plate separation the FSR decreases. So, one has to determine the optimum plate separation.

10 References

1. Ambastha, A., Hagyard, M. J. & West, E. A. 1993, *Solar Phys.*, **148**, 277.
2. Carlsson, M. & Stein, R. F. 1995, *ApJ*, **481**, 500.
3. Cavallini, F. 2006, *Solar Phys.*, **236**, 415.
4. Chae, J., Moon, Y -J., & Pevtsov, A. A. 2004, *ApJ*, **602**, L65.
5. Chen, H., & Jiang, Y. 2009, *Solar Phys.*, **255**, 79.
6. Cox, A. N. 2000, *Allen's Astrophysical Quantities*, IV edition, Springer-Verlag New York, Inc.
7. Darvann, T., & Owner-Petersen, M. 1994, *Prestudy of FPI filter for LEST*, LEST Technical Report 57.
8. de Wijn, A. G., Stenflo, J., Solanki, S., & Tsuneta, S. 2009, *Space Science Reviews*, **144**, 275.
9. Donea, A. -C. & Lindsey, C.: 2005, *ApJ*, **630**, 1168.
10. Gary, G. A., Balasubramaniam, K. S. & Sigwarth, M. 2002, *Multiple etalon system for the advanced technology solar telescope*, *ATST project documentation*.
11. Gilbert, H. R., Holzer, T. E., Burkepille, J. T., & Hundhausen, A. J. 2000, *ApJ*, **537**, 503.
12. Gosling, J. T. 1993, *JGR*, **98**, 18937.
13. Gupta, S. S. & Singh, Jagdev 1998, *BASI*, **26**, 203.
14. Hagyard, M. J., Stark, B. A., & Venkatakrishnan, P. 1999, , *Solar Phys.*, **184**, 133.
15. Hasan, S. S. & NLST team 2006, *Concept Proposal for a National Large Solar Telescope*, Submitted to DST, Government of India.
16. Jenkins, F. A. & White, H. E. 1937, *Fundamentals of Optics*, *McGraw-Hill international editions*".
17. Kumar, Brajesh & Ravindra, B. 2006, *JAA*, **27**, 425.
18. Kentischer, T. J., Schmidt, W., Sigwarth, M. & Uexküll, M. V. 1998, *A&A*, **340**, 569.
19. Li, H., Sakurai, T., Ichimoto, K., & Ueno, S. 2000, *PASJ*, **52**, 483.
20. Lites et al. 2008, *ApJ*, **672**, 1237.
21. Lites, B. W., Rutten, R. J. & Berger, T. E. 1999, *ApJ*, **517**, 1013.
22. Munro, R. H., Gosling, J. T., Hildner, E., MacQueen, R. M., Poland, A. I. & Ross, C. L. 1979, *Solar Phys.*, **61**, 201.
23. Prasad, S., & Dere, K. P. 2001, *ApJ*, **561**, 372.
24. Sakurai, T., Shibata, K., Ichimoto, K., Tsuneta, S. & Acton L. W. 1992, *PASJ*, **44**, L123.
25. Sankarasubramanian, K. 2010, *BASI*, in Press.
26. Singh, J. 2008, *JAA*, **29**, 345.
27. Sivaraman, K. R. & Livingston, W. C. 1982, *Solar Phys.*, **80**, 227.
28. Sivaraman, K. R., Gupta, S. S., & Livingston, W. C. et al. 2000, *A&A*, **307**, 288.
29. St. Cyr, O. C. & webb, D. F. 1991, *Solar Phys.*, **136**, 379.
30. Vecchio, A., Cauzzi, G., & Reardon, K. P. 2009, *A&A*, **494**, 269.
31. Wang, H., Ewell, M. W., Zirin, H., & Ai, G.: 1994 *ApJ*, **424**, 436.
32. Webb, D. F. & hundhausen, A. J. 1987, *Solar Phys.*, **108**, 383.
33. Xu, X., Fang, C., & Chen, P.: 2008, *CA&A*, **32**, 56.